ACS Catalysis

Research Article

Cite This: ACS Catal. 2019, 9, 3399−3412

pubs.acs.org/acscatalysis

Revealing the Synergy between Oxide and Alloy Phases on the Performance of Bimetallic In−Pd Catalysts for CO_2 Hydrogenation to Methanol

Jonathan L. Snider,[†] Verena Streibel,[†,‡] McKenzie A. Hubert,[†] Tej S. Choksi,[†,‡] Eduardo Valle,[†] D. Chester Upham,[†] Julia Schumann,[‡] Melis S. Duyar,[†,‡] Alessandro Gallo,*[,†,‡] Frank Abild-Pedersen,[‡] and Thomas F. Jaramillo*[,†,‡]

[†]SUNCAT Center for Interface Science and Catalysis, Department of Chemical Engineering, Stanford University, 443 Via Ortega, Stanford, California 94305, United States

[‡]SUNCAT Center for Interface Science and Catalysis, SLAC National Accelerator Laboratory, 2575 Sand Hill Road, Menlo Park, California 94025, United States

Supporting Information

ABSTRACT: In_2O_3 has recently emerged as a promising catalyst for methanol synthesis from CO_2. In this work, we present the promotional effect of Pd on this catalyst and investigate structure−performance relationships using *in situ* X-ray spectroscopy, *ex situ* characterization, and microkinetic modeling. Catalysts were synthesized with varying In:Pd ratios (1:0, 2:1, 1:1, 1:2, 0:1) and tested for methanol synthesis from CO_2/H_2 at 40 bar and 300 °C. In:Pd(2:1)/SiO_2 shows the highest activity (5.1 μmol MeOH/g_{InPd}s) and selectivity toward methanol (61%). While all bimetallic catalysts had enhanced catalytic performance, characterization reveals methanol synthesis was maximized when the catalyst contained both In−Pd intermetallic compounds and an indium oxide phase. Experimental results and density functional theory suggest the active phase arises from a synergy between the indium oxide phase and a bimetallic In−Pd particle with a surface enrichment of indium. We show that the promotion observed in the In−Pd system is extendable to non precious metal containing binary systems, in particular In−Ni, which displayed similar composition−activity trends to the In−Pd system. Both palladium and nickel were found to form bimetallic catalysts with enhanced methanol activity and selectivity relative to that of indium oxide.

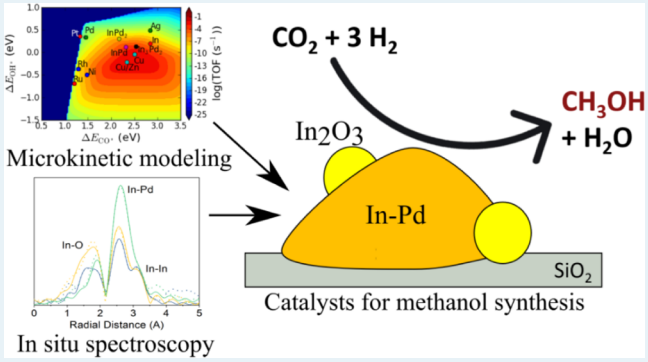

KEYWORDS: *In−Pd, In−Ni, In_2O_3, bimetallic, methanol synthesis, in situ characterization, CO_2 utilization, intermetallic*

INTRODUCTION

Mitigation of anthropogenic CO_2 production has become a major challenge due to the role of CO_2 as a significant greenhouse gas contributing to climate change and associated adverse environmental effects.[1,2] To address rising CO_2 concentrations, new processes to capture, sequester, and utilize carbon dioxide are needed. CO_2 utilization in particular is an attractive approach as it creates a value-added product while enabling carbon neutral or net negative emissions from a process.[3,4] Methanol synthesis is one promising pathway for CO_2 utilization due to its high volume production (60 megatonnes/year) and large-scale use as fuel, solvent, and platform chemical.[5,6]

Methanol is currently synthesized on $Cu/ZnO/Al_2O_3$ catalysts from syngas ($CO/CO_2/H_2$) at moderate temperatures (200−300 °C) and high pressures (50−100 bar).[7,8] This catalyst has been optimized for the CO-rich syngas ($CO/CO_2/H_2$) feed derived from steam reforming of methane and experiences deactivation as CO_2 concentration in the feed increases.[9−12] On $Cu/ZnO/Al_2O_3$ catalysts, CO hydrogenation is known to proceed through the formation of CO_2 via the water gas shift (WGS) reaction (eq 1), followed by hydrogenation of CO_2 to methanol (eq 2).[9,13−17]

$$CO + H_2O \leftrightarrow CO_2 + H_2 \quad (1)$$

$$CO_2 + 3H_2 \leftrightarrow CH_3OH + H_2O \quad (2)$$

At high concentrations of CO_2 in the feed, there is both a kinetic inhibition effect due to high coverages of adsorbates on the catalyst[9,17−19] as well as a significant sintering effect due to the presence of H_2O.[10,20] These limitations of the commercial $Cu/ZnO/Al_2O_3$ catalyst for direct CO_2 utilization motivate the search for new catalysts with favorable kinetics at high CO_2

Received: December 3, 2018
Revised: February 28, 2019
Published: March 8, 2019

DOI: 10.1021/acscatal.8b04848
ACS Catal. 2019, 9, 3399−3412

concentrations.[21−23]Recent work has shown that In_2O_3 is an attractive catalyst for methanol synthesis from CO_2 with methanol selectivities of up to 100% and increased comparative activity over $Cu/ZnO/Al_2O_3$.[24,25] Density functional theory (DFT) studies suggest that the activity of In_2O_3 is linked to oxygen vacancies in the oxide that can activate CO_2 molecules.[26,27] Subsequent work has showed that increasing the concentration of oxygen vacancies, such as by introducing Pd nanoparticles to form Pd/In_2O_3, can further increase methanol activity of the indium oxide.[28,29] Intermetallic In−Pd alloys have also been investigated for liquid phase methanol synthesis and were found to have enhanced activity over both pure In_2O_3 and pure Pd catalysts. While the presence of In_2O_3 was observed on the surface of these intermetallic catalysts, the relationship between surface oxide species and the intrinsic activity of the catalyst has not yet been elucidated.[30]

The relationship between a metal and support is complex, providing an opportunity to tune their interaction to improve catalytic performance. As discussed above, the metal can create defects in the support which can either be active sites for reaction[28,29] or can tune the electronic properties of the supported metal.[31,32] Additionally, alloying may occur between the metal and support, leading to the formation of a variety of intermetallic compounds of great interest to catalysis.[33,34] Finally, the presence of the support at the surface of the metal can lead to deactivation via encapsulation[35] or promotion at the metal−oxide interface.[36]

Pd/In_2O_3 and PdIn interactions have been studied across many reactions, including methanol steam reforming,[37−43] alcohol electrooxidation,[44,45] electrochemical carbon dioxide reduction,[46] ethane dehydrogenation,[47,48] acetylene hydrogenation,[49−51] nitrate reduction,[52] and methanol synthesis.[28−30] These mixed metal/oxide systems can enable unique reaction mechanisms compared to purely metallic systems.[21,28,53] In the case of methanol synthesis, an example is that of $PdGa/Ga_2O_3$ for CO_2 hydrogenation to methanol. The PdGa alloy site has been proposed to provide hydrogen via a spillover mechanism to reaction intermediates adsorbed at catalytic sites on the Ga_2O_3.[54] Methanol steam reforming (MSR), shown in eq 3, is also of particular interest as it is the reverse reaction of methanol synthesis.

$$CH_3OH + H_2O \leftrightarrow CO_2 + 3H_2 \quad (3)$$

Supported Pd−X (X = Zn, Ga, In, Sn, Ge) have shown great promise for the MSR reaction.[39,41] The combination of Pd with a reducible oxide has been shown to create intermetallic compounds which form unique metal−oxide and metal−metal interfaces. For PdZn, the catalyst promotion has been attributed to the formation of active, oxidized Zn species at the surface of a Zn-rich PdZn phase.[55,56] For $PdIn/In_2O_3$, the formation of a surface intermetallic compound was found to form an optimum bimetal−oxide synergy; however, strong metal−support interactions led to encapsulation by oxide and deactivation at higher temperatures.[42] However, subsequent studies have shown that the intermetallic alone is insufficient, as the active catalyst has a surface which is enriched in partially oxidized indium.[37] Even in complex, heterogeneous materials such as $GaPd_2/InPd/Ga_2O_3/In_2O_3$, the activity/selectivity is derived from optimized intermetallic-support phase boundaries.[43] In general, the results indicate the importance of these metal−oxide interfaces which play a fundamental role in the activation of reactants and intermediates. Due to the many phases present in these catalysts, it is crucial to characterize and understand the state of the catalyst under reaction conditions to understand which phases and interfaces contribute to the catalytic activity observed.

In the present work, we focus on silica supported In_2O_3, Pd, and In−Pd bimetallic catalysts for gas phase CO_2 hydrogenation to methanol and investigate the intrinsic activity of oxide and alloy phases. We employ transmission electron microscopy (TEM), X-ray diffraction (XRD), X-ray fluorescence (XRF), temperature-programmed reduction (TPR), *in situ* X-ray absorption spectroscopy (XAS), and density functional theory (DFT) with microkinetic modeling to reveal structure−activity relationships and the synergy between intermetallic compounds and oxide phases. We show that the coexistence of both indium oxide and Pd−In alloy phases results in promotion of the catalytic activity and selectivity toward methanol. We also present an In−Ni system, which is promising as a precious-metal-free catalyst for methanol synthesis and exhibits similar trends in activity.

METHODS

Catalyst Synthesis. Indium−palladium bimetallic catalysts were prepared using an incipient wetness impregnation (IWI) technique. Catalysts were prepared with varying In:Pd molar ratios (1:0, 2:1, 1:1, 1:2, 0:1), keeping the indium loading constant across the samples at 9 wt % In. For the monometallic Pd catalyst, an equivalent Pd loading to the 1:1 InPd catalyst was used (8.3 wt % Pd). In a typical procedure, indium(III) nitrate hydrate (Alfa Aesar, 40185) and palladium(II) nitrate dihydrate (Aldrich, 76070) were dissolved in 0.5 mL of Milli-Q water. The solution was then added dropwise to 0.5 g of Perkasil SM 660 silica powder (Grace Davison) and mixed. The resulting powder was dried overnight at 100 °C. The dried samples were then transferred to a muffle furnace to be calcined in air at 300 °C. The calcined catalysts were sieved to 180−300 μm size fraction and transferred to a catalytic reactor for further reduction and reaction steps.

Indium−nickel bimetallic catalysts with varying In:Ni molar ratios (2:1, 1:0.9, 1:2) were prepared by an analogous procedure starting from nickel(II) nitrate hexahydrate (Strem Chemicals, 28-1440).

Catalytic Testing. The performance of the catalysts for CO_2 hydrogenation was evaluated in a custom fixed bed reactor (BenchCAT 4000HP, Altamira Instruments). Hydrogen with a 2% argon internal standard, carbon dioxide, and nitrogen (ultrahigh purity grade, Airgas) were used as reactant and purge gases. In the reduction temperature survey, catalysts were reduced under 10% H_2/N_2 at 5 bar and various temperatures. Samples were then pressurized to 50 bar under nitrogen before switching to the reaction conditions: 50 bar, 300 °C, 130 sccm 4/1/1.5 $H_2/CO_2/N_2$ (GHSV: 63000 $cm^3/h/g_{cat}$). In the catalyst composition survey, catalysts were first reduced under 10% H_2/N_2 at 300 °C and 5 bar for 1 h. The samples were then pressurized to 40 bar under nitrogen before switching to the reaction conditions: 40 bar, 300 °C, 25 sccm 4/1 H_2/CO_2 (GHSV: 7500 $cm^3/h/g_{cat}$). A H_2:CO_2 ratio of 4 was used in these experiments as prior reports on indium oxide have found these conditions favorable for methanol synthesis.[29,57]

During the CO_2 hydrogenation reactions, products were regularly sampled and quantified with an on-stream gas chromatograph/mass spectrometer (Agilent 7890/5977) throughout the 10 h reactions. Product identities were confirmed by mass spectrometry, and products were quantified

DOI: 10.1021/acscatal.8b04848
ACS Catal. 2019, 9, 3399−3412

by flame ionization and thermal conductivity detector. All product lines were heated at or above 130 °C to prevent condensation of products in the lines. The carbon balance was checked and found to close as shown in the Supporting Information, Section 7.

After testing, catalyst powders were collected from the reactor and retained for postcatalysis characterizations.

Catalyst Characterization. Transmission electron microscopy (TEM) was performed on a FEI Tecnai G2 F20 X-TWIN to image the catalysts before and after catalytic testing. Sample powders were suspended in methanol and sonicated for 10 min before drop-casting onto lacey carbon TEM grids (Ted Pella, Inc.) to dry. Particle size histograms were derived from the images with at least 100 particles counted per sample. Surface area weighted average diameters were calculated using eq 4. A surface area weighting was selected in this work as heterogeneous catalysis and adsorbate binding are all surface phenomena.

$$d_{SA} = \frac{\sum_{di}^{3} n_i}{\sum_{di}^{2} n_i} \quad (4)$$

X-ray diffraction (XRD) was performed on a Rigaku MiniFlex 600 with a Kβ-filtered Cu Kα source (1.54 Å) and a D/teX Ultra detector. Continuous scans were collected between 2θ = 20−80° with a step size of 0.01° and a scan speed of 5°/min. Samples were analyzed both after calcination and after CO_2 hydrogenation. Samples were prepared by suspending the catalyst powders in isopropyl alcohol and drop-casting onto silicon sample holders to dry into a film. Crystallite sizes were calculated using the Scherrer equation, and measurement of NIST standards reveals instrument broadening to be negligible.

X-ray fluorescence (XRF) was performed on a Spectro Xepos HE XRF spectrometer. Roughly 0.1 g of catalyst powder was loaded for each measurement. Calculations were made using the instrument's "FP Alloys" setting based on first principles. Samples were analyzed both after calcination and after CO_2 hydrogenation with no significant difference observed between.

Temperature-programmed reduction (TPR) was performed on a custom analytical reactor (BenchCAT 1000RHP, Altamira Instruments). 10% H_2/Ar was used for the reduction, and the product gas was analyzed by an on-stream thermal conductivity detector. Temperatures were ramped at 10 °C/min.

In situ XAS was performed at beamline 9-3 at the Stanford Synchrotron Radiation Lightsource (SSRL). X-ray absorption near edge spectroscopy (XANES) and extended X-ray absorption fine structure (EXAFS) data were collected at the In and Pd K-edges (27.9 and 24.4 keV, respectively). Samples were measured under test conditions matching those of the catalytic tests described above. To enable measurement under reaction conditions, a custom gas delivery panel and packed bed flow reactor cell were utilized. The reactor, comprised of a heated beryllium tube, is capable of reaching temperatures of 500 °C and pressures of 50 bar. Each sample was loaded into the beryllium tube and purged with UHP Helium (Airgas) at room temperature and ambient pressure. In and Pd K-edge EXAFS were collected under these initial conditions. Then, a 10% H_2/He blend was introduced while the sample was heated to 300 °C (ramped at 5 °C/min) and pressurized to 5 bar. In K-edge XANES was collected during the ramp, and the samples were held at 300 °C until the spectra stopped changing (roughly 1 h), at which point In and Pd EXAFS were collected under the reduction conditions. Then, the reactor was maintained at 300 °C while being pressurized to 40 bar under a 4/1 H_2/CO_2 flow. EXAFS data were then collected at both the In and Pd K-edges under the reaction conditions. XAS analysis was performed using Athena and Artemis, part of the Demeter software package.[58] Additional details regarding the normalization and fitting process can be found in the Supporting Information.

XAS Simulations Using FEFF. XANES and EXAFS spectra were simulated with FEFF 9.[59] Crystallographic structures of pure Pd and In, as well as intermetallic compounds, were utilized. XANES simulations were conducted using an RPA-screened core hole for a SCF cluster of 7 Å and a FMS of 8 Å. The H-L self-energy was used for the calculation of the exchange correlation potential. For EXAFS calculations, only single scattering paths with a maximum distance of 6 Å and a global DW of 0.009 were considered. An additional experimental broadening of 1 eV was used. The simulated XANES spectra were aligned to the experimental ones.

Density Functional Theory and Microkinetic Modeling. Planewave density functional theory (DFT) calculations were performed using the Quantum ESPRESSO package[60] within the Atomic Simulation Environment (ASE).[61] The RPBE functional[62] was used to calculate self-consistent total energies. Core states were represented by ultrasoft Vanderbilt pseudopotentials.[63] The Kohn−Sham equations were solved in reciprocal space on a **k**-point grid generated with the Monkhorst−Pack scheme.[64] Spurious electrostatic interactions between periodic images were eliminated through a dipole correction applied perpendicular to the slab.[65] Adsorption energies of thermochemical descriptors for methanol synthesis (CO* and OH*) are referenced to gas phase energies of CH_4, H_2O, and H_2, consistent with previous work.[66] The methanol synthesis activity was evaluated on surfaces exposing low-coordinated sites for both monometallic In and Pd, along with experimentally observed intermetallic compounds In_3Pd_2 and InPd as well as $InPd_2$. Reactivity trends for In−Pd intermetallic compounds were determined using a previously published DFT-based mean-field microkinetic model.[9,66−69] Turnover frequencies were calculated under experimentally relevant conditions, i.e. 300 °C and 40 bar with a 4/1 H_2/CO_2 ratio, using the CatMAP software package.[70] Based on the resulting activity volcano, adsorption energies of CO* and OH* were used to determine the catalytic activity of the metals/intermetallic compounds. Further computational details are given in the Supporting Information.

RESULTS

X-ray Fluorescence (XRF). X-ray fluorescence was performed on the catalyst powders to confirm the ratios of In:Pd loaded onto the silica. The metal ratios are tabulated in Table 1. All catalysts exhibit a slight deficit of indium relative

Table 1. Elemental Composition of In−Pd Catalysts as Determined by X-ray Fluorescence

catalyst	nominal In/(In+Pd) (%)	measured In/(In+Pd) (%)
In:Pd(2:1)/SiO_2	66.7	63.8 ± 1.1
In:Pd(1:1)/SiO_2	50.0	48.1 ± 2.0
In:Pd(1:2)/SiO_2	33.3	30.9 ± 1.3

DOI: 10.1021/acscatal.8b04848
ACS Catal. 2019, 9, 3399−3412

to the nominal loadings, and no difference was observed between postcalcination and post-CO_2 hydrogenation measurements. For simplicity, the catalysts will be referred to by their nominal ratios, as in the table below, for the remainder of the manuscript.

Transmission Electron Microscopy. The morphology of the catalysts was analyzed with *ex situ* TEM, as shown in Figure 1. After calcination, the catalysts form dispersed nanoparticles.

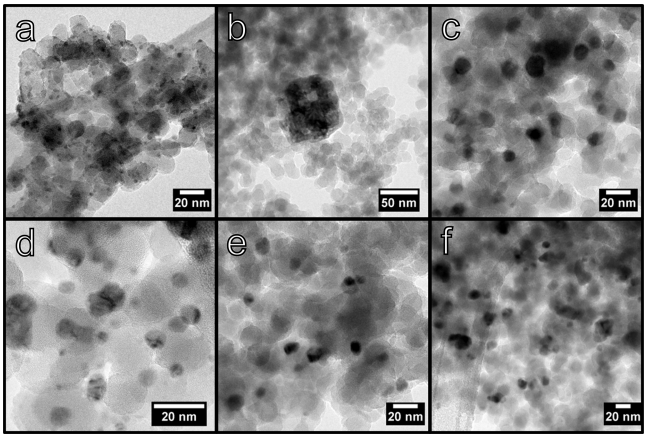

Figure 1. (a) Representative TEM image of the In:Pd(1:1)/SiO_2 catalyst after impregnation and calcination. TEM images after reduction and CO_2 hydrogenation for (b) In_2O_3/SiO_2, (c) In:Pd(2:1)/SiO_2, (d) In:Pd(1:1)/SiO_2, (e) In:Pd(1:2)/SiO_2, and (f) Pd/SiO_2.

A representative image from the In:Pd(1:1) catalyst is shown (Figure 1a). Sintering is observed after reduction and CO_2 hydrogenation, as evidenced by TEM of the spent catalysts (Figures 1b–f). Particle size distributions and surface area-weighted average diameters were determined for each catalyst as shown in Figure 2. In the case of pure In_2O_3, roughly cubic-shaped particles are observed with a d_{SA} of 86 nm. The introduction of Pd improves the dispersion of the catalysts significantly, as the d_{SA} of these catalysts drops to around 20 nm, and no particles larger than 50 nm were observed. Among the bimetallic samples, particle diameters and size distributions were similar.

Temperature Programmed Reduction. The supported In_2O_3, Pd, and In–Pd catalysts were evaluated with TPR to understand the effect of Pd on the In reducibility. Figure 3 shows the reduction behavior of each catalyst. Results for the monometallic catalysts are consistent with prior reports on In_2O_3 and PdO. For In_2O_3, there is a small feature at 280 °C which has previously been reported to arise from the formation of oxygen vacancies in the oxide.[24] As the temperature continues to rise up to 600 °C, the oxide gradually reduces as metallic indium forms.[37,57] It has been previously shown that supported indium oxide will begin reducing at temperatures between 500 and 700 °C.[71] In the case of Pd, the reduction of PdO to Pd occurs at room temperature in H_2, prior to the TPR measurement. We observe a negative peak corresponding to the release of H from β-PdH at 80 °C.[72]

Neither In:Pd(2:1) nor In:Pd(1:1) feature this hydride decomposition peak, demonstrating an absence of exposed Pd in the early phases of the reduction. The In:Pd(1:2) catalyst, on the other hand, does feature a negative peak around 90 °C, which is attributed to a PdH decomposition as in the Pd sample. This peak has also been observed on PdO/In_2O_3

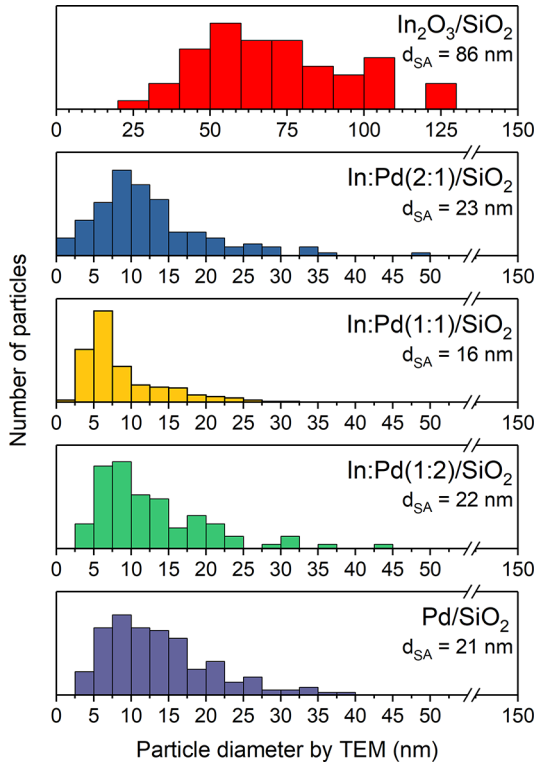

Figure 2. Particle size distributions for each In–Pd catalyst measured by *ex situ* TEM after performing CO_2 hydrogenation. Surface area-weighted average particle diameters (d_{SA}) are shown for each sample.

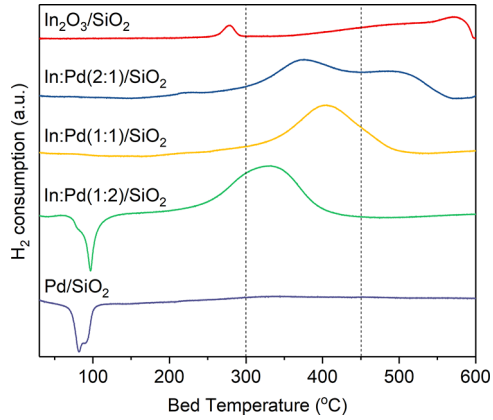

Figure 3. Temperature programmed reduction of the calcined In–Pd catalysts. Vertical lines depict the temperatures selected for the reduction temperature survey.

catalysts, where its identity as PdH decomposition was confirmed.[37] This feature is reflective of the increased Pd content in this catalyst and suggests the presence of monometallic Pd at the beginning of the reduction.

For the three bimetallic In–Pd catalysts, more complex behavior is observed. The calcined catalysts are initially present as In_2O_3 and PdO on SiO_2 (Supporting Information, Figure S8). As evidenced by the PdH features observed above, the PdO reduces during the pretreatment procedure prior to data collection. Pd first participates in the reduction of In_2O_3 to form the InPd intermetallic compound, as shown in prior studies of In–Pd reduction behavior.[37] Additionally, as we do not observe a feature near 600 °C on these catalysts, corresponding to In_2O_3 reduction to In metal, we conclude

DOI: 10.1021/acscatal.8b04848
ACS Catal. 2019, 9, 3399–3412

that a majority of the initial indium oxide participates in the formation of the intermetallic compounds.

In the In:Pd(1:1) and In:Pd(1:2) catalysts, only a single reduction feature is observed via TPR. These catalysts also feature a predominant InPd crystalline feature in XRD after CO_2 hydrogenation, to be discussed later. As such, this first peak for each bimetallic catalyst is attributed to the reaction of Pd with In_2O_3 to form InPd (eq 5). Prior work has shown that the reaction to form InPd is the first to occur during In−Pd intermetallic formation and occurs between 225 and 300 °C.[37] The shift to higher temperatures observed in Figure 3 can be due to differences in the test conditions (e.g., ramp rate) as well as differences in the sample compositions, PdO/In_2O_3 in ref 36 versus $PdO+In_2O_3/SiO_2$ in this work.

$$2Pd + 3H_2 + In_2O_3 \rightarrow 2InPd + 3H_2O \quad (5)$$

The In:Pd(2:1) sample has an additional peak at higher temperatures. It has been previously shown that the successive reaction after InPd formation is the further reduction of In_2O_3 to form the In_3Pd_2 intermetallic compound between 300 and 400 °C (eq 6), consistent with the phase we observe after CO_2 hydrogenation. This is followed by further reduction to form the In_7Pd_3 intermetallic compound above 425 °C.[37] However, at the lower pressures of hydrogen used in the TPR study (1 bar), higher temperatures might be required to achieve this phase. The XRF results (Table 1) show the In:Pd stoichiometry is insufficient to completely form bulk In_7Pd_3, so we assign the second peak to the formation of In_3Pd_2.

$$4InPd + 3H_2 + In_2O_3 \rightarrow 2In_3Pd_2 + 3H_2O \quad (6)$$

The TPR data demonstrate that the PdO readily reduces under mild conditions and that, at or above 300 °C, the bimetallic catalysts would all be expected to form a reduced phase to some extent. The reducibility of indium in the catalysts is found to vary as follows: $In_2O_3 \ll$ In:Pd(2:1) $\leq$ In:Pd(1:1) < In:Pd(1:2), showing that the presence of Pd facilitates In reduction.

CO_2 Hydrogenation: Reduction Temperature Survey. To determine the optimal reduction temperature for the In−Pd bimetallic catalysts, a survey was performed across various reduction temperatures. $In:Pd(1:1)/SiO_2$ was selected as a representative catalyst. A 300 °C reduction to match the reaction temperature was chosen as the lower bound, followed by 450 and 600 °C to sample regions within and beyond the reduction features observed in TPR. Steady state activity for CO_2 hydrogenation was evaluated at 50 bar, 300 °C and CO and methanol were detected as the only products. As shown in Figure 4 below, increasing the reduction temperature to form a further reduced phase leads to increased selectivity toward the reverse water−gas shift (RWGS) reaction and diminished methanol selectivity. While activity of the catalysts remains similar between 300 and 450 °C, going beyond the TPR features with a 600 °C reduction results in a dramatic drop in activity. TPR of the $In:Pd(1:1)/SiO_2$ sample up to 700 °C did not reveal additional reduction features at higher temperatures (Supporting Information, Figure S6), consistent with other reports on In−Pd intermetallic compounds.[37,39,49,52] Thus, the results of the reduction survey suggest that the presence of oxidized indium is important for CO_2 activation. Based on this reduction survey, subsequent studies were performed using the 300 °C reduction temperature for all catalysts to maximize methanol selectivity.

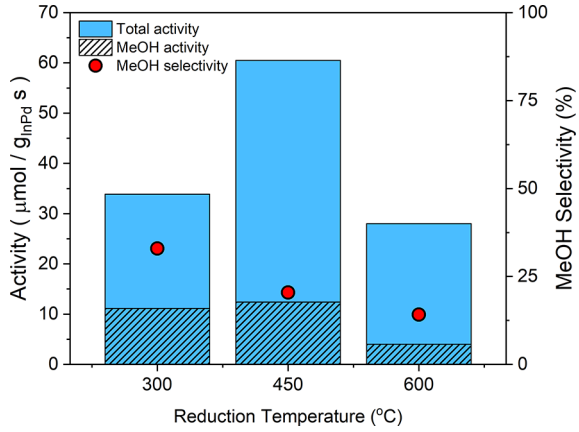

Figure 4. Activity and methanol selectivity of $In:Pd(1:1)/SiO_2$ reduced in 10% H_2/N_2 at varying temperatures (300, 450, and 600 °C). Steady-state data are shown for each individual reaction at 50 bar, 300 °C, and 130 sccm of 4/1/1.5 $H_2/CO_2/N_2$.

CO_2 Hydrogenation: Catalyst Composition Survey. Using the optimized reduction conditions, the different bimetallic catalysts were surveyed to determine the effect of the In:Pd ratio on the catalytic performance. Reaction conditions were selected (40 bar and 300 °C) to facilitate comparison to prior reports on In_2O_3 catalysts.[24,29] CO_2 hydrogenation activity and selectivity are plotted in Figure 5 and tabulated in Table 2 for monometallic and bimetallic In−Pd catalysts. In all cases, methanol and carbon monoxide accounted for over 97% of the products. Minor products included methane and dimethyl ether. Under these test conditions, the In_2O_3/SiO_2 control was found to have 24% selectivity toward methanol and a mass-normalized methanol activity of 0.9 μmol/g_{In}s. This selectivity is lower than some past reports on pure In_2O_3 catalysts;[57] however, it has been shown that methanol selectivity on In_2O_3 will decrease with decreasing space velocity,[27] and there are additional differences in our system (e.g., the SiO_2 support) which can influence the results. Introducing Pd into the catalyst has a dramatic effect on both activity and selectivity. All of the bimetallic catalysts had methanol activities greater than or equal to 2.9 μmol/g_{InPd}s. The $In:Pd(2:1)/SiO_2$ catalyst maximized both methanol activity (5.1 μmol/g_{InPd}s) and methanol selectivity (61%). Increasing the Pd:In ratio increased the total activity while lowering selectivity due to more CO being produced. The pure Pd catalyst showed the greatest CO activity at 10.8 μmol/g_{Pd}s and the lowest methanol activity.

To account for the size differences observed in TEM, surface area-normalized activities were also calculated for the five catalyst compositions (Figure 5b) using the surface-area weighted diameters determined by TEM. Note that, for the In_2O_3 catalyst, the TEM revealed large particles, while the XRD suggests a rougher, polycrystalline surface. As such, the surface-area-based activity for the In_2O_3 sample is an upper-bound, and the true activity is expected to be lower. Results show that the total activity of the catalysts does not change significantly when normalized with respect to the estimated surface area from TEM. Thus, the primary difference between the catalysts is the selectivity of active sites toward methanol. As shown in Table 2, the $In:Pd(2:1)/SiO_2$ catalyst is again found to have the greatest methanol activity (4.2×10^{-5} μmol/cm^2_{InPd}s).

DOI: 10.1021/acscatal.8b04848
ACS Catal. 2019, 9, 3399−3412

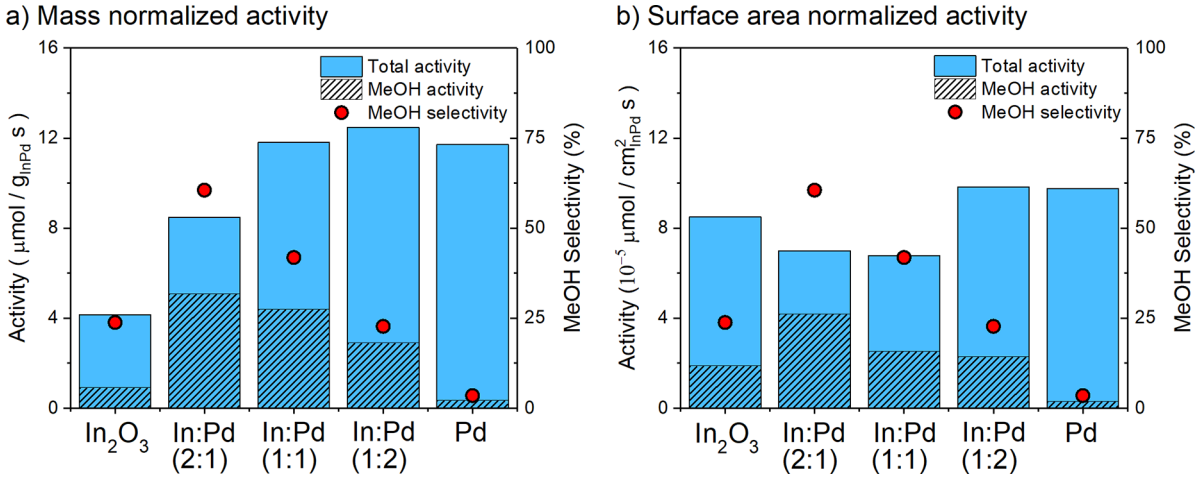

Figure 5. Steady-state activity and methanol selectivity of In−Pd/SiO_2 catalysts, averaged from multiple runs and normalized to either (a) the mass of In−Pd or (b) the estimated surface area from TEM. Catalysts were reduced at 300 °C in 10% H_2/N_2 prior to CO_2 hydrogenation at 40 bar, 300 °C, and 25 sccm of 4/1 H_2/CO_2.

Table 2. Key Methanol Synthesis Metrics for In−Pd/SiO_2 Catalysts Taken at Steady State[a]

sample	methanol selectivity (%)	mass-normalized methanol activity (μmol/g$_{InPd}$ s)	surface area-normalized methanol activity (μmol/cm$^2_{InPd}$ s))
In_2O_3/SiO_2	24	0.9	1.8×10^{-5}
In:Pd (2:1)/SiO_2	61	5.1	4.2×10^{-5}
In:Pd (1:1)/SiO_2	42	4.4	2.5×10^{-5}
In:Pd (1:2)/SiO_2	23	2.9	2.3×10^{-5}
Pd/SiO_2	4	0.4	0.3×10^{-5}

[a]Catalysts were reduced at 300 °C in 10% H_2/N_2 prior to CO_2 hydrogenation at 40 bar, 300°C, and 25 sccm of 4/1 H_2/CO_2.

X-ray Diffraction. X-ray diffraction of the catalysts after CO_2 hydrogenation reveals the final crystallographic structure of the samples (Figure 6). For the In_2O_3 catalyst, a cubic indium oxide structure was observed without any evidence for metallic In. The In:Pd(2:1) catalyst primarily forms an In_3Pd_2 intermetallic structure with some crystalline In_2O_3 remaining. Small shoulders appear to the left of the primary In_3Pd_2 peaks, indicating a minor InPd phase. The In:Pd(1:1) catalyst forms a single InPd intermetallic compound. In:Pd(1:2) also features predominant InPd peaks alongside a minor, more Pd-rich fcc structure. The shoulder and unlabeled peaks featured on In:Pd(1:2) coincide closely with the peaks of the Pd fcc structure; however, they are shifted to smaller angles due to the addition of the larger indium atoms into the compound. Finally, the monometallic Pd catalyst forms crystalline Pd metal.

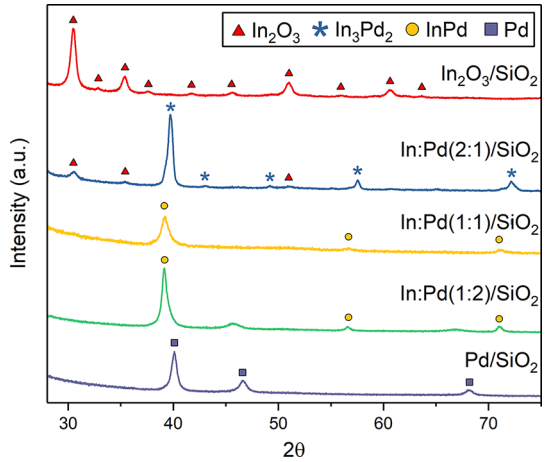

Figure 6. X-ray diffraction patterns of In−Pd catalysts after CO_2 hydrogenation. Reference peaks are noted for the major phases observed: In_2O_3,[75] In_3Pd_2,[76] InPd,[76] and Pd.[77]

These results may initially appear in contrast to the In−Pd phase diagram which shows a great variety of thermodynamically stable phases within our range of compositions.[73] Prior work has observed that when forming In−Pd intermetallic compounds, the InPd cubic structure is formed first due to its crystallographic similarity to the Pd fcc structure.[48] This might be expected given that palladium is the first to reach its metallic state as shown by TPR. The XRD results also agree well with the XRF data, as we observe Pd enrichment in the catalysts and In:Pd(2:1) and In:Pd(1:2) both contain minor Pd-rich intermetallic compounds.

Average crystallite sizes were calculated by the Scherrer equation[74] and are tabulated in Table 3. For the Pd-containing catalysts, the size determined by XRD (9.8−16.8 nm) is consistent with the size observed by TEM (8.7−14 nm). For the In_2O_3 catalyst, the crystallite size remains small at 14.1 nm while the TEM revealed much larger particles up to 130 nm, suggesting these larger In_2O_3 structures are polycrystalline. To provide the most conservative comparison to the intermetallic compounds, the particle size as determined by TEM was used for the normalized activities shown in Table 2 above.

Density Functional Theory and Microkinetic Modeling. We assessed the intrinsic methanol synthesis activity of the In−Pd intermetallic compounds using a DFT derived microkinetic model. The resulting activity map for methanol production as a function of the descriptors ΔECO* and ΔE_{OH*}, which is based on a model constructed previously and detailed in prior work,[66] is shown in Figure 7. The feed is composed of CO_2 and H_2 (8 and 32 bar, respectively), and the

DOI: 10.1021/acscatal.8b04848
ACS Catal. 2019, 9, 3399−3412

Table 3. Structure and Size of In−Pd Crystallites as Determined by X-ray Diffraction and Transmission Electron Microscopy[a]

sample	major phase	avg crystallite size (XRD) (nm)	avg particle size (TEM) (nm)	surface area-weighted average particle size (TEM) (nm)
In_2O_3/SiO_2	bixybite In_2O_3	14.1	71	86
In:Pd (2:1)/SiO_2	In_3Pd_2	14.8	13	23
In:Pd (1:1)/SiO_2	InPd	9.8	8.7	16
In:Pd (1:2)/SiO_2	InPd	16.8	13	22
Pd/SiO_2	Pd	14.3	14	21

[a]Average crystallite size calculated from the Scherrer equation.

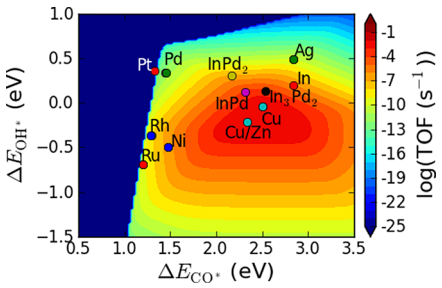

Figure 7. Activity maps for transition metal and In−Pd intermetallic compounds for methanol synthesis from CO_2 and H_2 on surfaces exposing low-coordinated sites. TOFs are determined as a function of adsorption energies of CO* and OH* (ΔECO* and ΔE_{OH*}, respectively). T = 300 °C, $p(CO_2)$ = 8 bar, $p(H_2)$ = 32 bar. Adsorption energies of CO* and OH* are referenced relative to gas-phase energies of CH_4, H_2O, and H_2.

temperature is 300 °C. From the activity map, we can estimate the turnover frequency (TOF) of methanol synthesis as a function of the CO* and OH* adsorption energies of the different materials. Figure 7 shows that with increasing Pd content, the In−Pd intermetallic compounds bind CO* more strongly. The OH* adsorption energy is only slightly impacted, with InPd and In_3Pd_2 showing the strongest OH* binding. We observe that the moderate addition of Pd to In (up to 50%) moves the material toward the peak of the activity map, i.e. to higher methanol synthesis TOFs. A too large Pd content, however, is detrimental to the methanol synthesis activity because the material adsorbs carbon-bound intermediates too strongly as in the case of $InPd_2$. In agreement with our experimental observations, InPd and In_3Pd_2 are shown in Figure 7 to have methanol synthesis activities intrinsically higher than those of pure Pd and the Pd-rich $InPd_2$ intermetallic.

***In situ* X-ray Absorption Spectroscopy.** *Palladium Extended X-ray Absorption Fine Structure.* To understand the properties of the In−Pd catalysts which drive catalytic performance, *in situ* XAS was collected under the reaction conditions used above (40 bar, 300 °C, 4/1 H_2/CO_2). Data from the Pd K-edge is shown in Figure 8 for each catalyst under various *in situ* conditions. The Fourier transform of the EXAFS region was fit to PdO, InPd, or In_3Pd_2 crystallographic structures, giving the parameters shown in Table 4.

After impregnation and calcination, all catalysts have similar PdO features. The radial distances from the fits are all consistent with PdO standards and prior reports.[78,79] The coordination numbers, consistent among the sample series, correspond to values lower than that of bulk PdO, confirming the nanostructure of the materials.[80] Upon switching to the reduction conditions (300 °C, 5 bar, H_2), all the samples exhibit a complete reduction of the PdO phase. It was not possible to deconvolute the Pd−In path from the Pd−Pd path, and, as such, it has been defined as a generic Pd-M (where M = In, Pd) scattering path. In all cases, the best fit was achieved using the cubic CsCl-type InPd crystalline structure.[81] For In:Pd(2:1), the radial distance was found to be 2.77 Å, consistent with In−Pd intermetallic compounds synthesized in the literature.[48,49,82] For the other bimetallic catalysts, In:Pd(1:1) and In:Pd(1:2), a radial distance of 2.75 Å was fit under the reduction conditions. This distance falls between that of metallic Pd (2.74 Å)[78,79] and InPd (2.81 Å).[48,81,82] This

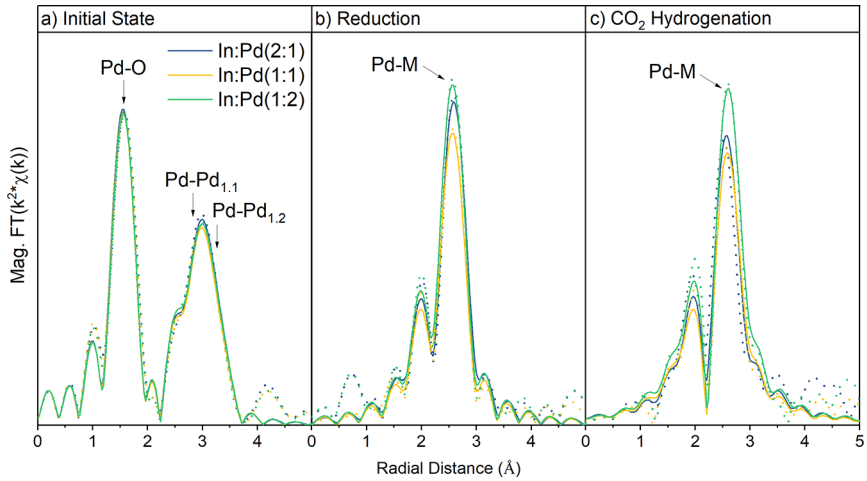

Figure 8. *In situ* Pd K-edge EXAFS collected on the In−Pd/SiO_2 catalyst samples under the (a) initial conditions (25 °C, 1 bar, He), (b) reduction conditions (300 °C, 5 bar, H_2), and (c) CO_2 hydrogenation (300 °C, 40 bar, 4/1 H_2/CO_2) conditions. In:Pd(2:1)/SiO_2 is shown in blue, In:Pd(1:1)/SiO_2 in yellow, and In:Pd(1:2)/SiO_2 in green. Dotted lines depict the experimental data, while the solid lines show the fitted model.

DOI: 10.1021/acscatal.8b04848
ACS Catal. 2019, 9, 3399−3412

Table 4. Coordination Numbers (CN), Radial Distances (R), and Debye−Waller factors (DW) Determined by EXAFS Fitting of the Pd K-edge of In−Pd Catalysts Measured under Initial, Reduction, and CO_2 Hydrogenation Conditions.[a]

		25 °C, He, 1 bar			300 °C, H_2, 5 bar			300 °C, 4/1 H_2/CO_2, 40 bar		
sample	path	CN	R (Å)	DW (10^{-3})	CN	R (Å)	DW (10^{-3})	CN	R (Å)	DW (10^{-3})
In:Pd(2:1)/SiO_2	Pd−O	4.3	2.01	1						
	Pd−M	2.0; 2.8	3.02; 3.45	1	8.1	2.77	12	7.4*	2.76*	13*
In:Pd(1:1)/SiO_2	Pd−O	4.2	2.01	1						
	Pd−M	1.9; 2.5	3.02; 3.44	1	6.4	2.75	11	6.3	2.77	12
In:Pd(1:2)/SiO_2	Pd−O	4.1	2.01							
	Pd−M	1.9; 2.6	3.02; 3.45	1	7.6	2.75	11	7.8	2.77	12

[a]Fitting was performed using the In_2O_3 and InPd crystal structures. *Fit using the In_3Pd_2 structure.

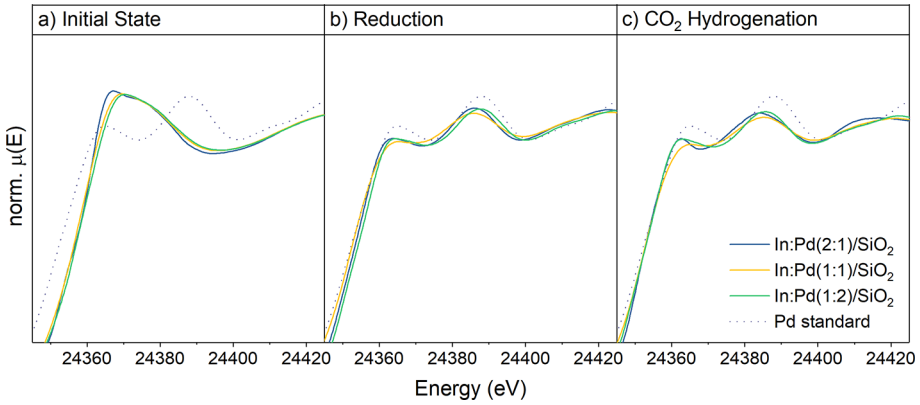

Figure 9. *In situ* Pd K-edge XANES collected under the (a) initial conditions (25 °C, 1 bar, He), (b) reduction conditions (300 °C, 5 bar, H_2), and (c) CO_2 hydrogenation (300 °C, 40 bar, 4/1 H_2/CO_2) conditions for the In:Pd(2:1) (blue), In:Pd(1:1) (yellow), and In:Pd(1:2) (green) catalysts. Experimental spectra are compared against a measured Pd standard (dotted).

intermediate value suggests an incomplete incorporation of In into the reduced phase.

Spectra collected under reaction conditions (300 °C, 40 bar, 4/1 H_2/CO_2) again show a complete reduction of the Pd. The Pd−M radial distance found under CO_2 hydrogenation for all bimetallic samples was 2.76−2.77 Å. This increase in radial distance is consistent with the formation of In−Pd intermetallic compounds, which have been found experimentally to have radial distances between 2.76 and 2.80.[48,49,82] Within this range of radial distances, the smaller distances are associated with more Pd-rich intermetallic phases or mixtures of phases.[48] Thus, based on the measured radial distance, the samples contain additional phases not observed by XRD. Additionally, the increase in radial distance observed under CO_2 hydrogenation reveals that additional indium is incorporated into the intermetallic compound under the higher hydrogen pressures of the reaction conditions.

The coordination numbers do not vary significantly between reduction and reaction or among the sample series, and they are consistent with the nanoparticulate morphology observed via TEM. It is also important to note the absence of the higher coordination shells, consistent with the high temperatures of the in situ measurement,[83] as well as the sample properties such as size and disorder.[84−86] This impact of this on the XAS measurements, as well as additional differences between our samples and fully stoichiometric compounds, is discussed further in the Supporting Information. In general, from the perspective of the Pd EXAFS, the catalysts all appear strikingly similar, despite the different stoichiometry and crystalline structures observed. Pd XANES, as will be discussed next, also shows similar Pd features across the catalysts. These similarities in the Pd features suggest that differences in the indium component of the catalysts are driving the observed differences in reactivity.

Palladium X-ray Absorption Near Edge Structure. The Pd XANES region provides information about the oxidation state and structure of Pd within the catalyst and demonstrates the formation of intermetallic compounds. Upon the introduction of hydrogen, there is a clear shift from Pd^{2+} to Pd^0 (Figures 9a and b) evidenced by the drop in the white line intensity and the rise of peaks mirroring the Pd standard spectrum. The XANES structure observed on the bimetallic samples has small deviations from the Pd standard, in agreement with the EXAFS results presented above. Upon continuing to the reaction conditions, the XANES spectra shift further from the Pd standard consistent with the incorporation of additional indium as shown in EXAFS. The shift of the features to lower energies is consistent with FEFF simulations of various In−Pd intermetallic compounds (Supporting Information, Figure S2) and literature reports on other In−Pd intermetallic compounds.[48,82] Thus, the XANES is consistent with the incorporation of indium into the palladium, as observed in XRD.

Comparing the measured spectra with the FEFF simulations reveals that the differences observed in the spectra can arise from the formation of different intermetallic compounds in the samples. However, the structure observed in XANES is more consistent with the structure of more Pd-rich intermetallic compounds (Figure S2). This is in agreement with the radial distances observed in EXAFS and again show that our samples are a heterogeneous mixture of phases, including some more Pd-like than those observed in XRD.

Indium Extended X-ray Absorption Fine Structure. While the Pd edge showed very consistent results from sample to

DOI: 10.1021/acscatal.8b04848
ACS Catal. 2019, 9, 3399−3412

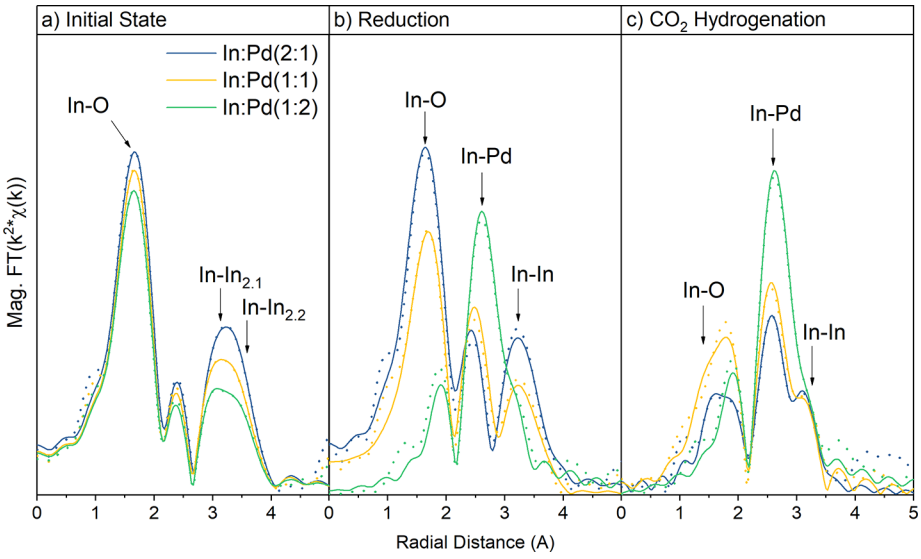

Figure 10. *In situ* In K-edge EXAFS collected on the In−Pd catalyst samples under the (a) initial conditions (25 °C, 1 bar, He), (b) reduction conditions (300 °C, 5 bar, H_2), and (c) CO_2 hydrogenation (300 °C, 40 bar, 4:1 H_2/CO_2) conditions. In:Pd(2:1)/SiO_2 is shown in blue, In:Pd(1:1)/SiO_2 in yellow, and In:Pd(1:2)/SiO_2 in green. Dotted lines depict the experimental data, while the solid lines show the fitted model.

Table 5. Coordination Numbers (CN), Radial Distances (R), and Debye−Waller factors (DW) Determined by EXAFS Fitting of the In K-edge of In−Pd Catalysts Measured under Initial, Reduction, and CO_2 Hydrogenation Conditions[a]

		25 °C, He, 1 bar			300 °C, H_2, 5 bar			300 °C, 4/1 H_2/CO_2, 40 bar		
sample	path	CN	*R* (Å)	DW (10^{-3})	CN	*R* (Å)	DW (10^{-3})	CN	*R* (Å)	DW (10^{-3})
In_2O_3/SiO_2	In−O	6.3	2.17	6	7.1	2.16	12	7.1	2.16	12
	In−In	5.8; 3.6	3.35; 3.81	6	6.7; 4.4	3.35; 3.79	12	6.6; 4.4	3.35; 3.79	12
In:Pd(2:1)/SiO_2	In−O	6.3	2.16	6	5.5	2.14	11	0.6	2.13	4
	In−Pd				1.6	2.76	11	1.8*	2.75*	7*
	In−In	5.7; 3.6	3.35; 3.82	6	6.5; 5.1	3.32; 3.77	11	1.9; 2.1*	2.86; 3.36*	10; 16*
In:Pd(1:1)/SiO_2	In−O	6.0	2.16	6	3.9	2.16	11	2.9	2.11	15
	In−Pd				2.3	2.74	11	4.4	2.78	15
	In−In	4.8; 2.8	3.34; 3.81	6	2.75; 3.0	3.32; 3.80	11	1.7	3.34	15
In:Pd(1:2)/SiO_2	In−O	5.6	2.16	6						
	In−Pd				5.9	2.75	13	7.0	2.76	15
	In−In	3.8; 2.3	3.35; 3.81	6	1.9	3.26	13	1.8	3.23	15

[a]Fitting was performed using the In_2O_3 and InPd crystal structures. *Fit using the In_3Pd_2 structure.

sample, *in situ* XAS at the indium edge reveals differences in catalyst structure. The Fourier transform of the EXAFS region was fit to In_2O_3 (bixbyite),[87] InPd (cubic CsCl-type),[81] or In_3Pd_2 (hexagonal Al_3Ni_2-type)[81] crystallographic structures. These results for the bimetallic catalysts are shown in Figure 10, while the fitting of the In_2O_3/SiO_2 catalyst can be found in Figure S4 of the Supporting Information.

Initially, the catalysts are found to be fully oxidized. The radial distances all match the bixbyite cubic In_2O_3 structure,[88] and the coordination numbers are consistent with the presence of nanoparticles as before. Under the reduction conditions, varying degrees of reduction are observed from sample to sample. Following the In−O coordination, shown in Table 5, it can be seen that the oxide fraction decreases as the Pd:In ratio increases, and it is completely absent for In:Pd(1:2). This decrease coincides with the emergence of a new path in the EXAFS, which can be fit to the first In−Pd shell of the InPd structure. The radial distances fit for this path vary between 2.74 and 2.76 Å. As was seen in the Pd EXAFS above, these values fall between those observed in a metallic Pd lattice and an intermetallic InPd lattice. While In:Pd(1:2) is dominated by this new path, In:Pd(2:1) and In:Pd(1:1) still maintain significant In−O coordination. Under the reaction conditions, indium is further reduced under the higher pressure of hydrogen. While the In−Pd path intensity increases relative to the In−O path, In:Pd(2:1) and In:Pd(1:1) maintain a mixture of oxide and intermetallic compounds, even under the reaction conditions. In:Pd(1:2), on the other hand, solely contains intermetallic compounds. The reduced radial distance for In−O in the In:Pd(1:1) sample is consistent with prior reports on amorphous In_2O_3,[88] consistent with the XRD results which do not reveal crystalline In_2O_3. The radial distance of In−Pd increases for all bimetallic samples to be consistent with In−Pd intermetallic compounds found in literature, with In−Pd lengths of 2.75−2.80 Å.[48,82] This agreement again demonstrates the incorporation of additional indium into the intermetallic compound to form the final intermetallic compounds observed after catalysis.

The coordination numbers determined at the In K-edge also give additional insights into the structure of the catalysts. N_{In-Pd} for the In:Pd(2:1) catalyst (1.8), and to a lesser extent the In:Pd(1:1) catalyst (4.4), are smaller than the N_{Pd-In}

DOI: 10.1021/acscatal.8b04848
ACS Catal. 2019, 9, 3399−3412

observed at the Pd K-edge (7.8). Compared to fully stoichiometric compounds, decreased coordination numbers are expected for catalysts consisting of a mixture of oxide phases with the intermetallic compounds, as observed in our samples, because the measured coordination is normalized to the entirety of the catalyst.[47,48] However, an under-coordinated indium environment such as at the particle surface, can also reduce the observed coordination numbers. The fully reduced In:Pd(1:2) catalyst (N_{In-Pd} = 7) is still found to have a smaller In−Pd coordination than the N_{Pd-In} of 7.8 measured at the Pd edge. The small decrease observed on In:Pd(1:2) could again signify an enrichment of In near the surface; however, it is within the expected errors found in EXAFS.[89]

To probe this possibility in more depth, CO chemisorption was performed on the catalysts (Supporting Information, Table S5). A dramatic drop in CO uptake was observed on samples with increased indium content, with the In:Pd(2:1) sample having no detectable CO uptake. Our electronic structure calculations show that on the InPd intermetallic compounds, CO only adsorbs on Pd sites with a decreasing interaction strength between CO and the surface as the In content increases (compare Figure 7 and Section 1 of the Supporting Information). The calculations further show that CO does not adsorb on metallic In. These theoretical results have already been demonstrated experimentally as well for In−Pd intermetallic compounds, CO has been found to only adsorbed on surface Pd sites, while metallic indium and indium oxide have not been found to adsorb CO under these conditions.[47,48,90] Because the particle size remains similar across the four Pd-containing samples in the series, the dramatic drop in CO uptake that is greater than what one would expect based on stoichiometry alone suggests that the surfaces of In:Pd(1:1)/SiO_2 and In:Pd(2:1)/SiO_2 are enriched in non-CO adsorbing indium species (metallic or oxide).

Indium X-ray Absorption Near Edge Structure. As with the EXAFS results above, the indium XANES region also shows more dynamic behavior than at the Pd-edge. The spectra are found to change significantly with either the reactor conditions or catalyst compositions. In general, as the reduction and then reaction conditions are reached, the white-line intensity decreases as the samples transition from In^{3+} to a lower average indium oxidation state. The XANES spectra under each condition can be found in the Supporting Information (Figure S3). The final state of the catalyst is initially difficult to ascertain, as the sample contains a mixture of oxide and intermetallic compounds which need to be deconvoluted. To understand the mixing of the phases in more detail, we applied linear combination fitting to each In XANES spectrum. First, we assumed that the intermetallic compounds present are similar, due to the striking similarities observed in the Pd XAS data. To represent this phase, we selected the In:Pd(1:2)/SiO_2 catalyst under reaction conditions, where no oxide component was observed in the indium EXAFS. Then, we assumed that the oxide phases are also similar and can be represented by the In_2O_3/SiO_2 catalyst prior to reduction. Fitting the remaining catalysts between these two extremes, we get the results shown in Figure 11. Interestingly, both In:Pd(2:1) and In:Pd(1:1) approach the same final In_2O_3 content under reaction conditions despite large differences observed during the low pressure reduction step. The XANES results confirm that, under CO_2 hydrogenation conditions, the In:Pd(2:1) and In:Pd(1:1) catalysts exist as mixtures of indium oxide and In−Pd intermetallic compounds and further suggests that these

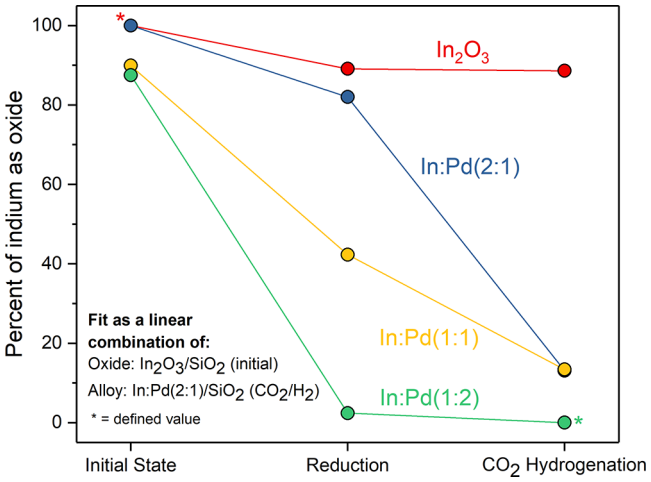

Figure 11. Linear combination fitting of indium K-edge XANES for the In−Pd/SiO_2 catalysts under ambient (25 °C, He, 1 bar), reduction (300 °C, 10% H_2/He, 5 bar), and CO_2 hydrogenation (300 °C, 40 bar, 4:1 H_2/CO_2) conditions. The In_2O_3/SiO_2 ambient spectrum and In:Pd(1:2)/SiO_2 CO_2 hydrogenation spectrum were defined as the principle components.

two catalysts have a similar percentage of the indium present in an oxidized state.

Elucidating the Promotional Effect in In−Pd Catalysts. Specific methanol activity and methanol selectivity are maximized in the In:Pd(2:1) sample at 4.2 × 10^{-5} μmol/cm^2_{InPd}s and 61% selectivity. XAS and XRD revealed this sample is predominantly composed of an In_3Pd_2 intermetallic compound and indium oxide. The In:Pd(1:1) sample, on the other hand, produced 2.5 × 10^{-5} μmol/cm^2_{InPd}s of methanol at 42% selectivity. This sample contained primarily the InPd intermetallic compound and an amorphous or highly disperse indium oxide. Finally, the In:Pd(1:2) sample produced 2.3 × 10^{-5} μmol/cm^2_{InPd}s of methanol at only 23% selectivity. This sample only contained intermetallic compounds of In−Pd.

From theory, we predict the intrinsic methanol activity of the intermetallic compounds to be higher than either pure metal catalysts due to more favorable CO* and OH* adsorption energies. Indeed, this promotion is observed as all three bimetallic samples have greater methanol activities than the Pd/SiO_2 catalyst. However, this alone does not account for the promotion trends observed. The results also indicate a correlation between the presence of an oxide phase and improved selectivity toward methanol. On both the In:Pd(2:1) and In:Pd(1:1) samples, CO chemisorption revealed that the surfaces of the catalysts are enriched in indium with In:Pd(2:1) having no detectable CO uptake (Table S5). As Pd surface sites are associated with both CO adsorption and higher WGS activity,[84,91,92] this agrees well with the selectivity trends observed on the samples. Based on the dramatically different performance between the oxide-containing In:Pd(2:1) and In:Pd(1:1) samples though, the oxide appears to be playing a larger role than simply blocking Pd sites.

Work on related catalysts reveals the significance of the oxide-alloy interface in promoting catalysis. For instance, it has been previously shown that Pd can promote the formation of oxygen vacancies in indium oxide catalysts for methanol synthesis.[28,29] As these vacancies have favorable binding for CO_2,[26,27] this creates additional active sites for the reaction. Thus, the oxide must be considered as a potential active site

DOI: 10.1021/acscatal.8b04848
ACS Catal. 2019, 9, 3399−3412

and not merely as a site-blocker. Relevant work on the methanol steam reforming (MSR), offers some additional perspective. It has been observed that ZnPd/ZnO catalysts have high CO_2 selectivity when the ZnPd particles are partially oxidized with time on stream. The formation of ZnO patches creates a synergistic ZnPd-ZnO interface.[55] A similar promotion process has also been proposed for $InPd/In_2O_3$ catalysts for MSR. During MSR conditions, it was observed that the intermetallic particles became enriched at the surface with oxidized indium species, which correlated with enhanced performance.[37] Thus, based on the experimental data presented herein and the rich literature available on this class of material, we conclude that the coexistence of In−Pd intermetallic compounds and indium oxide enhances the methanol synthesis performance of these catalysts, with methanol synthesis occurring at a synergistic interface between the intermetallic and oxide phases. Furthermore, we conclude that the In:Pd(2:1) sample, containing indium oxide and an In_3Pd_2 intermetallic compound with a surface enrichment in indium, created the most synergistic interface of the sample series.

Expanding the Phase Space: In−Ni Catalysts. The results above reveal a significant promotional effect upon the addition of Pd to In-based catalysts for methanol synthesis. We hypothesized that similar promotional effects could be achieved in other In-based intermetallic compounds. To test this hypothesis, we prepared several In−Ni catalysts as described below. The results motivate additional investigations into this and other indium intermetallic compounds for methanol synthesis.

The selection of In−Ni is based on the design principles explored in the In−Pd investigation above. Pd is thought to facilitate alloy and oxygen vacancy formation in In_2O_3, which has been associated with improved methanol synthesis performance.[28−30] Thus, nickel might be expected to perform similarly as it can also readily dissociate H atoms[93] and can form various intermetallic compounds with In.[94] As such, we investigated In−Ni as an alternative, precious metal free catalyst to In−Pd. Results for CO_2 hydrogenation (300 °C, 40 bar, 4:1 H_2/CO_2) with the In−Ni catalysts are shown in Figure 12.

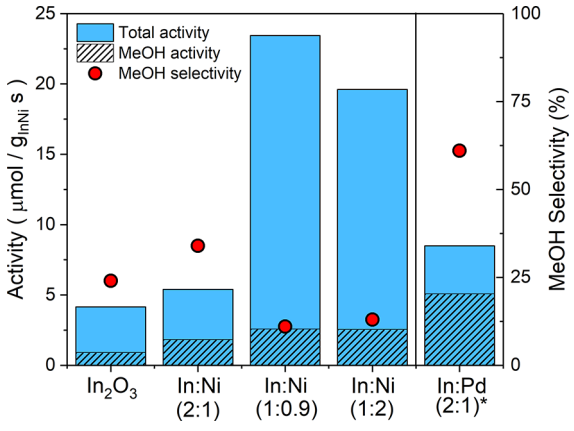

Figure 12. Steady-state activity and methanol selectivity of In−Ni/SiO_2 catalysts. Catalysts were reduced at 300 °C in 10% H_2/N_2 prior to CO_2 hydrogenation at 40 bar, 300 °C, and 25 sccm of 4/1 H_2/CO_2. *In:Pd(2:1) is normalized to the total mass of InPd.

The bimetallic catalysts again produced more methanol than the pure indium oxide catalyst, consistent with the In−Pd results discussed previously. Selectivity was maximized on the In:Ni(2:1) catalyst (34%) which had the highest indium content of the sample series, again consistent with the trends observed with In−Pd. Methanol activity was maximized on the In:Ni(1:0.9) catalyst (2.6 μmol/g_{InNi}s); however, there was less variation in methanol activity among the three In−Ni samples. While the In−Ni catalysts showed a promotion over the supported In_2O_3 catalyst, they had lower methanol activity and selectivity than the In−Pd catalysts, reflective of the less noble character of Ni. Interestingly, both the In−Ni and the In−Pd catalysts showed little to no activity for methanation, with less than 1% selectivity to methane. Given nickel's propensity for CO_2 methanation under similar conditions,[95,96] this suggests that monometallic nickel particles are absent from the In−Ni catalysts. This preliminary investigation suggests that the promotion effects can be extended beyond In−Pd systems. This presents opportunities for further development of In-based bimetallic catalysts prepared with nickel or other transition metals.

CONCLUSIONS

Bimetallic In−Pd and In−Ni catalysts with varying metal ratios were synthesized, characterized, and tested for methanol synthesis. All of the bimetallic In−Pd catalysts show enhanced specific methanol activity over the monometallic Pd and In_2O_3 catalysts, with In:Pd(2:1)/SiO_2 being the highest at 5.1 μmol/g_{InPd}s. The highest methanol selectivity achieved was 61% with the In:Pd(2:1)/SiO_2 catalyst, from which point increasing the Pd content decreased the methanol selectivity. Theory investigations corroborate this finding by showing how alloying In with Pd results in highly active methanol synthesis catalysts. *In situ* XAS characterization further revealed that a synergistic effect between an indium oxide phase and an indium−palladium intermetallic compound can further enhance methanol synthesis activity and selectivity. The active phase is proposed to be a bimetallic In−Pd particle with a surface enrichment of indium species that has synergy with an indium oxide phase. Similar promotional effects are observed in a non precious metal containing In−Ni/SiO_2 system, suggesting the promotion mechanism is translatable to other alloy/oxide systems and warrants further study.

ASSOCIATED CONTENT

Supporting Information

The Supporting Information is available free of charge on the ACS Publications website at DOI: 10.1021/acscatal.8b04848.

Details of DFT modeling and EXAFS fitting, additional XAS of In−Pd/SiO_2 and In_2O_3 catalysts, XAS FEFF simulations, additional XRD analysis, carbon balance, CO chemisorption, high temperature TPR measurement, and ICDD references for XRD standards (PDF)

Tabulated data for graphs presented (XLSX)

AUTHOR INFORMATION

Corresponding Authors

*E-mail: jaramillo@stanford.edu; Phone: +01 (650) 498-6879 (T.F.J.).

*E-mail: agallo@slac.stanford.edu (A.G.).

ORCID

Tej S. Choksi: 0000-0002-9520-019X

DOI: 10.1021/acscatal.8b04848
ACS Catal. 2019, 9, 3399−3412

Melis S. Duyar: 0000-0002-9891-5932
Alessandro Gallo: 0000-0003-4687-8188
Frank Abild-Pedersen: 0000-0002-1911-074X
Thomas F. Jaramillo: 0000-0001-9900-0622

Notes

The authors declare no competing financial interest.

■ ACKNOWLEDGMENTS

Primary support by the U.S. Department of Energy Office of Basic Energy Sciences to the SUNCAT Center for Interface Science and Catalysis is gratefully acknowledged. Support for Jonathan L. Snider was provided by the National Science Foundation Graduate Research Fellowship under Grant DGE-114747. V.S. gratefully acknowledges financial support from the Alexander von Humboldt Foundation. TEM was performed at the Stanford Nano Shared Facilities (SNSF) at Stanford University, supported by the National Science Foundation under award ECCS-1542152. XRD and XRF were performed at the Environmental Measurements Facility (EMF) at Stanford University. Use of the Stanford Synchrotron Radiation Lightsource, SLAC National Accelerator Laboratory, is supported by the U.S. Department of Energy, Office of Basic Energy Sciences under Contract DE-AC02-76SF00515. Technical support from SSRL staff, Matthew Latimer, and Erik Nelson during experiments at SSRL Experimental Station 9-3 is greatly appreciated.

■ REFERENCES

(1) Chu, S.; Majumdar, A. Opportunities and Challenges for a Sustainable Energy Future. *Nature* **2012**, *488*, 294−303.
(2) Friedlingstein, P.; Andrew, R. M.; Rogelj, J.; Peters, G. P.; Canadell, J. G.; Knutti, R.; Luderer, G.; Raupach, M. R.; Schaeffer, M.; Van Vuuren, D. P.; Le Quere, C. Persistent Growth of CO_2 Emissions and Implications for Reaching Climate Targets. *Nat. Geosci.* **2014**, *7*, 709−715.
(3) Hunt, A. J.; Sin, E. H. K.; Marriott, R.; Clark, J. H. Generation, Capture, and Utilization of Industrial Carbon Dioxide. *ChemSusChem* **2010**, *3*, 306−322.
(4) Yu, K. M. K.; Curcic, I.; Gabriel, J.; Tsang, S. C. E. Recent Advances in CO_2 Capture and Utilization. *ChemSusChem* **2008**, *1*, 893−899.
(5) Olah, G. A. After Oil and Gas: Methanol Economy. *Catal. Lett.* **2004**, *93*, 1−2.
(6) Olah, G. A.; Goeppert, A.; Prakash, G. K. S. Beyond Oil and Gas: The Methanol Economy: Second Edition. *Beyond Oil Gas Methanol Econ. Second Ed.* **2009**, 1−334.
(7) Graciani, J.; Mudiyanselage, K.; Xu, F.; Baber, A. E.; Evans, J.; Senanayake, S. D.; Stacchiola, D. J.; Liu, P.; Hrbek, J.; Sanz, J. F.; Rodriguez, J. A. Highly Active Copper-Ceria and Copper-Ceria-Titania Catalysts for Methanol Synthesis from CO_2. *Science* **2014**, *345*, 546−550.
(8) Behrens, M.; Studt, F.; Kasatkin, I.; Kühl, S.; Hävecker, M.; Abild-Pedersen, F.; Zander, S.; Girgsdies, F.; Kurr, P.; Kniep, B.; Tovar, M.; Fischer, R. W.; Nørskov, J. K.; Schlögl, R. The Active Site of Methanol Synthesis over $Cu/ZnO/Al_2O_3$ Industrial Catalysts. *Science* **2012**, *336*, 893−897.
(9) Studt, F.; Behrens, M.; Kunkes, E. L.; Thomas, N.; Zander, S.; Tarasov, A.; Schumann, J.; Frei, E.; Varley, J. B.; Abild-Pedersen, F.; Nørskov, J. K.; Schlögl, R. The Mechanism of CO and CO_2 Hydrogenation to Methanol over Cu-Based Catalysts. *ChemCatChem* **2015**, *7*, 1105−1111.
(10) Sahibzada, M.; Metcalfe, I. S.; Chadwick, D. Methanol Synthesis from $CO/CO_2/H_2$ over $Cu/ZnO/Al_2O_3$ at Differential and Finite Conversions. *J. Catal.* **1998**, *174*, 111−118.
(11) Schack, C. J.; McNeil, M. A.; Rinker, R. G. Methanol Synthesis from Hydrogen, Carbon Monoxide, and Carbon Dioxide over a $CuO/ZnO/Al_2O_3$ Catalyst. I. Steady-State Kinetics Experiments. *Appl. Catal.* **1989**, *50*, 247−263.
(12) Klier, K.; Chatikavanij, V.; Herman, R. G.; Simmons, G. W. Catalytic Synthesis of Methanol from CO/H_2 IV. The Effects of Carbon Dioxide. *J. Catal.* **1982**, *74*, 343−360.
(13) Zhang, Y.; Sun, Q.; Deng, J.; Wu, D.; Chen, S. A High Activity $Cu/ZnO/Al_2O_3$ Catalyst for Methanol Synthesis: Preparation and Catalytic Properties. *Appl. Catal., A* **1997**, *158*, 105−120.
(14) Yang, Y.; Mims, C. A.; Mei, D. H.; Peden, C. H. F.; Campbell, C. T. Mechanistic Studies of Methanol Synthesis over Cu from $CO/CO_2/H_2/H_2O$ Mixtures: The Source of C in Methanol and the Role of Water. *J. Catal.* **2013**, *298*, 10−17.
(15) Lee, J. S.; Lee, K. H.; Lee, S. Y.; Kim, Y. G. A Comparative Study of Methanol Synthesis from CO_2/H_2 and CO/H_2 over a $Cu/ZnO/Al_2O_3$ Catalyst. *J. Catal.* **1993**, *144*, 414−424.
(16) Liu, G.; Willcox, D.; Garland, M.; Kung, H. The Role of CO_2 in Methanol Synthesis on Cu-Zn Oxide: An Isotope Labeling Study. *J. Catal.* **1985**, *96*, 251−260.
(17) Grabow, L. C.; Mavrikakis, M. Mechanism of Methanol Synthesis on Cu through CO_2 and CO Hydrogenation. *ACS Catal.* **2011**, *1*, 365−384.
(18) Sun, Q.; Liu, C.-W.; Pan, W.; Zhu, Q.-M.; Deng, J.-F. In Situ IR Studies on the Mechanism of Methanol Synthesis over an Ultrafine $Cu/ZnO/Al_2O_3$ Catalyst. *Appl. Catal., A* **1998**, *171*, 301−308.
(19) Askgaard, T. S.; Nørskov, J. K.; Ovesen, C. V.; Stoltze, P. A Kinetic Model of Methanol Synthesis. *J. Catal.* **1995**, *156*, 229−242.
(20) Martin, O.; Pérez-Ramírez, J. New and Revisited Insights into the Promotion of Methanol Synthesis Catalysts by CO_2. *Catal. Sci. Technol.* **2013**, *3*, 3343−3352.
(21) Rodriguez, J. A.; Liu, P.; Stacchiola, D. J.; Senanayake, S. D.; White, M. G.; Chen, J. G. Hydrogenation of CO_2 to Methanol: Importance of Metal-Oxide and Metal-Carbide Interfaces in the Activation of CO_2. *ACS Catal.* **2015**, *5*, 6696−6706.
(22) Liu, X.-M.; Lu, G. Q.; Yan, Z.-F.; Beltramini, J. Recent Advances in Catalysts for Methanol Synthesis via Hydrogenation of CO and CO_2. *Ind. Eng. Chem. Res.* **2003**, *42*, 6518−6530.
(23) Wang, J.; Li, G.; Li, Z.; Tang, C.; Feng, Z.; An, H.; Liu, H. A Highly Selective and Stable $ZnO-ZrO_2$ Solid Solution Catalyst for CO_2 Hydrogenation to Methanol. *Sci. Adv.* **2017**, 1−11.
(24) Martin, O.; Martín, A. J.; Mondelli, C.; Mitchell, S.; Segawa, T. F.; Hauert, R.; Drouilly, C.; Curulla-Ferré, D.; Pérez-Ramírez, J. Indium Oxide as a Superior Catalyst for Methanol Synthesis by CO_2 Hydrogenation. *Angew. Chem., Int. Ed.* **2016**, *55*, 6261−6265.
(25) Sun, K.; Fan, Z.; Ye, J.; Yan, J.; Ge, Q.; Li, Y.; He, W.; Yang, W.; Liu, C. J. Hydrogenation of CO_2 to Methanol over In_2O_3 Catalyst. *J. CO2 Util.* **2015**, *12*, 1−6.
(26) Ye, J.; Liu, C.; Mei, D.; Ge, Q. Active Oxygen Vacancy Site for Methanol Synthesis from CO_2 Hydrogenation on In2O3(110): A DFT Study. *ACS Catal.* **2013**, *3*, 1296−1306.
(27) Ye, J.; Liu, C.; Ge, Q. DFT Study of CO_2 Adsorption and Hydrogenation on the In_2O_3 Surface. *J. Phys. Chem. C* **2012**, *116*, 7817−7825.
(28) Ye, J.; Liu, C. J.; Mei, D.; Ge, Q. Methanol Synthesis from CO_2 Hydrogenation over a Pd_4/In_2O_3 Model Catalyst: A Combined DFT and Kinetic Study. *J. Catal.* **2014**, *317*, 44−53.
(29) Rui, N.; Wang, Z.; Sun, K.; Ye, J.; Ge, Q.; Liu, C. CO_2 Hydrogenation to Methanol over Pd/In_2O_3Effects of Pd and Oxygen Vacancy. *Appl. Catal., B* **2017**, *218*, 488−497.
(30) García-Trenco, A.; Regoutz, A.; White, E. R.; Payne, D. J.; Shaffer, M. S. P.; Williams, C. K. PdIn Intermetallic Nanoparticles for the Hydrogenation of CO_2 to Methanol. *Appl. Catal., B* **2018**, *220*, 9−18.
(31) Cao, Y.; Maitarad, P.; Gao, M.; Taketsugu, T.; Li, H.; Yan, T.; Shi, L.; Zhang, D. Defect-Induced Efficient Dry Reforming of Methane over Two-Dimensional Ni/h-Boron Nitride Nanosheet Catalysts. *Appl. Catal., B* **2018**, *238*, 51−60.

DOI: 10.1021/acscatal.8b04848
ACS Catal. 2019, 9, 3399−3412

(32) Lu, M.; Fang, J.; Han, L.; Faungnawakij, K.; Li, H.; Cai, S.; Shi, L.; Jiang, H.; Zhang, D. Coke-Resistant Defect-Confined Ni-Based Nanosheet-like Catalysts Derived from Halloysites for CO_2 Reforming of Methane. *Nanoscale* **2018**, *10*, 10528−10537.
(33) Penner, S.; Armbrüster, M. Formation of Intermetallic Compounds by Reactive Metal − Support Interaction : A Frequently Encountered Phenomenon in Catalysis. *ChemCatChem* **2015**, *7*, 374−392.
(34) Armbrüster, M.; Schlögl, R.; Grin, Y. Intermetallic Compounds in Heterogeneous Catalysis - A Quickly Developing Field. *Sci. Technol. Adv. Mater.* **2014**, *15*, 034803.
(35) Gubó, R.; Yim, C. M.; Allan, M.; Pang, C. L.; Berkó, A.; Thornton, G. Variation of SMSI with the Au:Pd Ratio of Bimetallic Nanoparticles on TiO_2(110). *Top. Catal.* **2018**, *61*, 308−317.
(36) Sun, D.; Gu, X.-K.; Ouyang, R.; Su, H.-Y.; Fu, Q.; Bao, X.; Li, W.-X. Theoretical Study of the Role of a Metal−Cation Ensemble at the Oxide−Metal Boundary on CO Oxidation. *J. Phys. Chem. C* **2012**, *116*, 7491−7498.
(37) Neumann, M.; Teschner, D.; Knop-Gericke, A.; Reschetilowski, W.; Armbrüster, M. Controlled Synthesis and Catalytic Properties of Supported In-Pd Intermetallic Compounds. *J. Catal.* **2016**, *340*, 49−59.
(38) Men, Y.; Kolb, G.; Zapf, R.; O'Connell, M.; Ziogas, A. Methanol Steam Reforming over Bimetallic Pd-In/Al_2O_3 Catalysts in a Microstructured Reactor. *Appl. Catal., A* **2010**, *380*, 15−20.
(39) Iwasa, N.; Mayanagi, T.; Ogawa, N.; Sakata, K.; Takezawa, N. New Catalytic Functions of Pd-Zn, Pd-Ga, Pd-In, Pt-Zn, Pt-Ga and Pt-In Alloys in the Conversions of Methanol. *Catal. Lett.* **1998**, *54*, 119−123.
(40) Rameshan, C.; Lorenz, H.; Mayr, L.; Penner, S.; Zemlyanov, D.; Arrigo, R.; Haevecker, M.; Blume, R.; Knop-Gericke, A.; Schlögl, R.; Klötzer, B. CO_2-Selective Methanol Steam Reforming on In-Doped Pd Studied by in Situ X-Ray Photoelectron Spectroscopy. *J. Catal.* **2012**, *295*, 186−194.
(41) Lorenz, H.; Rameshan, C.; Bielz, T.; Memmel, N.; Stadlmayr, W.; Mayr, L.; Zhao, Q.; Soisuwan, S.; Klötzer, B.; Penner, S. From Oxide-Supported Palladium to Intermetallic Palladium Phases: Consequences for Methanol Steam Reforming. *ChemCatChem* **2013**, *5*, 1273−1285.
(42) Lorenz, H.; Turner, S.; Lebedev, O. I.; Van Tendeloo, G.; Klötzer, B.; Rameshan, C.; Pfaller, K.; Penner, S. Pd-In_2O_3 Interaction Due to Reduction in Hydrogen: Consequences for Methanol Steam Reforming. *Appl. Catal., A* **2010**, *374*, 180−188.
(43) Rameshan, C.; Lorenz, H.; Armbrüster, M.; Kasatkin, I.; Klötzer, B.; Götsch, T.; Ploner, K.; Penner, S. Impregnated and Co-Precipitated Pd−Ga_2O_3Pd−In_2O_3 and Pd−Ga_2O_3−In_2O_3 Catalysts: Influence of the Microstructure on the CO_2 Selectivity in Methanol Steam Reforming. *Catal. Lett.* **2018**, *148*, 3062−3071.
(44) Serov, A.; Martinez, U.; Atanassov, P. Novel Pd-In Catalysts for Alcohols Electrooxidation in Alkaline Media. *Electrochem. Commun.* **2013**, *34*, 185−188.
(45) Chu, D.; Wang, J.; Wang, S.; Zha, L.; He, J.; Hou, Y.; Yan, Y.; Lin, H.; Tian, Z. High Activity of Pd-In_2O_3/CNTs Electrocatalyst for Electro-Oxidation of Ethanol. *Catal. Commun.* **2009**, *10*, 955−958.
(46) White, J. L.; Bocarsly, A. B. Enhanced Carbon Dioxide Reduction Activity on Indium-Based Nanoparticles. *J. Electrochem. Soc.* **2016**, *163*, 410−416.
(47) Wegener, E. C.; Wu, Z.; Tseng, H.-T.; Gallagher, J. R.; Ren, Y.; Diaz, R. E.; Ribeiro, F. H.; Miller, J. T. Structure and Reactivity of Pt−In Intermetallic Alloy Nanoparticles: Highly Selective Catalysts for Ethane Dehydrogenation. *Catal. Today* **2018**, *299*, 146−153.
(48) Wu, Z.; Wegener, E. C.; Tseng, H. T.; Gallagher, J. R.; Harris, J. W.; Diaz, R. E.; Ren, Y.; Ribeiro, F. H.; Miller, J. T. Pd-In Intermetallic Alloy Nanoparticles: Highly Selective Ethane Dehydrogenation Catalysts. *Catal. Sci. Technol.* **2016**, *6*, 6965−6976.
(49) Smirnova, N. S.; Shlyapin, D. A.; Protasova, O. V.; Trenikhin, M. V.; Gulyaeva, T. I.; Gerasimov, E. Y.; Kibis, L. S.; Shitova, N. B.; Kochubey, D. I.; Tsyrul'nikov, P. G. Investigation of Active Component State in Pd/Ga_2O_3 and Pd/In_2O_3 Catalysts for Liquid-Phase Hydrogenation of Acetylene to Ethylene. *Chem. Sustain. Dev.* **2013**, *21*, 91−100.
(50) Cao, Y.; Sui, Z.; Zhu, Y.; Zhou, X.; Chen, D. Selective Hydrogenation of Acetylene over Pd-In/Al_2O_3 Catalyst: Promotional Effect of Indium and Composition-Dependent Performance. *ACS Catal.* **2017**, *7*, 7835−7846.
(51) Luo, Y.; Alarcón, S.; Friedrich, M.; Teschner, D.; Knop-Gericke, A.; Armbrüster, M. Addressing Electronic Effects in the Semi-Hydrogenation of Ethyne by $InPd_2$ and Intermetallic Ga−Pd Compounds. *J. Catal.* **2016**, *338*, 265−272.
(52) Witońska, I.; Karski, S.; Rogowski, J.; Krawczyk, N. The Influence of Interaction between Palladium and Indium on the Activity of Pd-In/Al_2O_3 Catalysts in Reduction of Nitrates and Nitrites. *J. Mol. Catal. A: Chem.* **2008**, *287*, 87−94.
(53) Dal Santo, V.; Gallo, A.; Naldoni, A.; Guidotti, M.; Psaro, R. Bimetallic Heterogeneous Catalysts for Hydrogen Production. *Catal. Today* **2012**, *197*, 190−205.
(54) Collins, S. E.; Delgado, J. J.; Mira, C.; Calvino, J. J.; Bernal, S.; Chiavassa, D. L.; Baltanás, M. A.; Bonivardi, A. L. The Role of Pd-Ga Bimetallic Particles in the Bifunctional Mechanism of Selective Methanol Synthesis via CO2 Hydrogenation on a Pd/Ga_2O_3 Catalyst. *J. Catal.* **2012**, *292*, 90−98.
(55) Friedrich, M.; Penner, S.; Heggen, M.; Armbrüster, M. High CO_2 Selectivity in Methanol Steam Reforming through ZnPd/ZnO Teamwork. *Angew. Chem., Int. Ed.* **2013**, *52*, 4389−4392.
(56) Friedrich, M.; Teschner, D.; Knop-Gericke, A.; Armbrüster, M. Influence of Bulk Composition of the Intermetallic Compound ZnPd on Surface Composition and Methanol Steam Reforming Properties. *J. Catal.* **2012**, *285*, 41−47.
(57) Martin, O.; Martín, A. J.; Mondelli, C.; Mitchell, S.; Segawa, T. F.; Hauert, R.; Drouilly, C.; Curulla-Ferré, D.; Pérez-Ramírez, J. Indium Oxide as a Superior Catalyst for Methanol Synthesis by CO_2 Hydrogenation. *Angew. Chem., Int. Ed.* **2016**, *55*, 6261−6265.
(58) Ravel, B.; Newville, M. ATHENA, ARTEMIS, HEPHAESTUS: Data Analysis for X-Ray Absorption Spectroscopy Using IFEFFIT. *J. Synchrotron Radiat.* **2005**, *12*, 537−541.
(59) Rehr, J. J.; Kas, J. J.; Vila, F. D.; Prange, M. P.; Jorissen, K. Parameter-Free Calculations of X-Ray Spectra with FEFF9. *Phys. Chem. Chem. Phys.* **2010**, *12*, 5503−5513.
(60) Giannozzi, P.; Baroni, S.; Bonini, N.; Calandra, M.; Car, R.; Cavazzoni, C.; Ceresoli, D.; Chiarotti, G. L.; Cococcioni, M.; Dabo, I.; Dal Corso, A.; De Gironcoli, S.; Fabris, S.; Fratesi, G.; Gebauer, R.; Gerstmann, U.; Gougoussis, C.; Kokalj, A.; Lazzeri, M.; Martin-Samos, L.; Marzari, N.; Mauri, F.; Mazzarello, R.; Paolini, S.; Pasquarello, A.; Paulatto, L.; Sbraccia, C.; Scandolo, S.; Sclauzero, G.; Seitsonen, A. P.; Smogunov, A.; Umari, P.; Wentzcovitch, R. M. QUANTUM ESPRESSO: A Modular and Open-Source Software Project for Quantum Simulations of Materials. *J. Phys.: Condens. Matter* **2009**, *21*, 395502.
(61) Larsen, A. H.; Mortensen, J. J.; Blomqvist, J.; Castelli, I. E.; Christensen, R.; Dułak, M.; Friis, J.; Groves, M. N.; Hammer, B.; Hargus, C.; Hermes, E. D.; Jennings, P. C.; Jensen, P. B.; Kermode, J.; Kitchin, J. R.; Kolsbjerg, E. L.; Kubal, J.; Kaasbjerg, K.; Lysgaard, S.; Maronsson, J. B.; Maxson, T.; Olsen, T.; Pastewka, L.; Peterson, A.; Rostgaard, C.; Schiøtz, J.; Schütt, O.; Strange, M.; Thygesen, K. S.; Vegge, T.; Vilhelmsen, L.; Walter, M.; Zeng, Z.; Jacobsen, K. W. The Atomic Simulation Environment — a Python Library for Working with Atoms. *J. Phys.: Condens. Matter* **2017**, *29*, 273002.
(62) Hammer, B.; Hansen, L. B.; Norskov, J. K. Improved Adsorption Energetics within Density-Functional Theory Using Revised Perdew-Burke-Ernzerhof. *Phys. Rev. B: Condens. Matter Mater. Phys.* **1999**, *59*, 7413−7421.
(63) Vanderbilt, D. Soft Self-Consistent Pseudopotentials in a Generalized Eigenvalue Formalism. *Phys. Rev. B: Condens. Matter Mater. Phys.* **1990**, *41*, 7892−7895.
(64) Monkhorst, H. J.; Pack, J. D. Special Points for Brillouin-Zone Integrations. *Phys. Rev. B* **1976**, *13*, 5188−5192.

DOI: 10.1021/acscatal.8b04848
ACS Catal. 2019, 9, 3399−3412

(65) Bengtsson, L. Dipole Correction for Surface Supercell Calculations. *Phys. Rev. B: Condens. Matter Mater. Phys.* **1999**, *59*, 12301−12304.
(66) Duyar, M.; Tsai, C.; Snider, J. L.; Singh, J. A.; Gallo, A.; Yoo, J. S.; Medford, A. J.; Abild-Pedersen, F.; Studt, F.; Kibsgaard, J.; Bent, S.; Nørskov, J. K.; Jaramillo, T. Discovery of a Highly Active Molybdenum Phosphide Catalyst for Methanol Synthesis from CO and CO_2. *Angew. Chem., Int. Ed.* **2018**, *57*, 15045−15050.
(67) Yoo, J. S.; Abild-Pedersen, F.; Norskov, J. K.; Studt, F. Theoretical Analysis of Transition-Metal Catalysts for Formic Acid Decomposition. *ACS Catal.* **2014**, *4*, 1226−1233.
(68) Studt, F.; Sharafutdinov, I.; Abild-Pedersen, F.; Elkjær, C. F.; Hummelshøj, J. S.; Dahl, S.; Chorkendorff, I.; Nørskov, J. K. Discovery of a Ni-Ga Catalyst for Carbon Dioxide Reduction to Methanol. *Nat. Chem.* **2014**, *6*, 320−324.
(69) Medford, A. J.; Lausche, A. C.; Abild-Pedersen, F.; Temel, B.; Schjødt, N. C.; Nørskov, J. K.; Studt, F. Activity and Selectivity Trends in Synthesis Gas Conversion to Higher Alcohols. *Top. Catal.* **2014**, *57*, 135−142.
(70) Medford, A. J.; Shi, C.; Hoffmann, M. J.; Lausche, A. C.; Fitzgibbon, S. R.; Bligaard, T.; Nørskov, J. K. CatMAP: A Software Package for Descriptor-Based Microkinetic Mapping of Catalytic Trends. *Catal. Lett.* **2015**, *145*, 794−807.
(71) Chen, M.; Xu, J.; Liu, Y. M.; Cao, Y.; He, H. Y.; Zhuang, J. H. Supported Indium Oxide as Novel Efficient Catalysts for Dehydrogenation of Propane with Carbon Dioxide. *Appl. Catal., A* **2010**, *377*, 35−41.
(72) Fagherazzi, G.; Benedetti, A.; Polizzi, S.; Di Mario, A.; Pinna, F.; Signoretto, M.; Pernicone, N. Structural Investigation on the Stoichiometry of β-PdH_x in Pd/SiO_2 Catalysts as a Function of Metal Dispersion. *Catal. Lett.* **1995**, *32*, 293−303.
(73) Okamoto, H. In-Pd (Indium-Palladium). *J. Phase Equilib.* **2003**, *24*, 481−481.
(74) Patterson, A. L. The Scherrer Formula for X-Ray Particle Size Determination. *Phys. Rev.* **1939**, *56*, 978−982.
(75) Marezio, M. Refinement of the Crystal Structure of In_2O_3 at Two Wavelengths. *Acta Crystallogr.* **1966**, *20*, 723−728.
(76) Hellner, E.; Laves, F. Kristallchemie Des In Und Ga in Legierungen Mit Einigen Übergangselementen (Ni, Pd, Pt, Cu, Ag Und Au). *Z. Naturforsch., A: Phys. Sci.* **1947**, *2*, 177−184.
(77) Rudnitskii, A. A.; Polyakova, R. S. The Palladium-Ruthenium System. *Russ. J. Inorg. Chem.* **1959**, *4*, 631.
(78) Hackett, S. F. J.; Brydson, R. M.; Gass, M. H.; Harvey, I.; Newman, A. D.; Wilson, K.; Lee, A. F. High-Activity, Single-Site Mesoporous Pd/Al_2O_3 Catalysts for Selective Aerobic Oxidation of Allylic Alcohols. *Angew. Chem.* **2007**, *119*, 8747−8750.
(79) Miller, H. A.; Lavacchi, A.; Vizza, F.; Marelli, M.; Di Benedetto, F.; D'Acapito, F.; Paska, Y.; Page, M.; Dekel, D. R. A $Pd/C\text{-}CeO_2$ Anode Catalyst for High-Performance Platinum-Free Anion Exchange Membrane Fuel Cells. *Angew. Chem.* **2016**, *128*, 6108−6111.
(80) Marinkovic, N.; Sasaki, K.; Adzic, R. Nanoparticle Size Evaluation of Catalysts by EXAFS: Advantages and Limitations. *Zast. Mater.* **2016**, *57*, 101−109.
(81) Harris, I. R.; Norman, M.; Bryant, A. W. A Study of Some Palladium-Indium, Platinum-Indium, and Platinum-Tin Alloys. *J. Less-Common Met.* **1968**, *16*, 427−440.
(82) Feng, Q.; Zhao, S.; Wang, Y.; Dong, J.; Chen, W.; He, D.; Wang, D.; Yang, J.; Zhu, Y.; Zhu, H.; Gu, L.; Li, Z.; Liu, Y.; Yu, R.; Li, J.; Li, Y. Isolated Single-Atom Pd Sites in Intermetallic Nanostructures: High Catalytic Selectivity for Semihydrogenation of Alkynes. *J. Am. Chem. Soc.* **2017**, *139*, 7294−7301.
(83) Rockenberger, J.; Eychmüller, A.; Kornowski, A.; Vossmeyer, T.; Feldhaus, J.; Tröger, L.; Weller, H. EXAFS Studies on the Size Dependence of Structural and Dynamic Properties of CdS Nanoparticles. *J. Phys. Chem. B* **1997**, *101*, 2691−2701.
(84) Groppo, E.; Navarro Yerga, R. M.; Kunkes, E. L.; Poceiro, B.; Kasatkin, I.; Behrens, M.; Ota, A.; Ferri, D. Comparative Study of Hydrotalcite-Derived Supported Pd_2Ga and PdZn Intermetallic Nanoparticles as Methanol Synthesis and Methanol Steam Reforming Catalysts. *J. Catal.* **2012**, *293*, 27−38.
(85) Cheng, G.; Carter, J. D.; Guo, T. Investigation of Co Nanoparticles with EXAFS and XANES. *Chem. Phys. Lett.* **2004**, *400*, 122−127.
(86) Sun, Y.; Frenkel, A. I.; Isseroff, R.; Shonbrun, C.; Forman, M.; Shin, K.; Koga, T.; White, H.; Zhang, L.; Zhu, Y.; Rafailovich, M. H.; Sokolov, J. C. Characterization of Palladium Nanoparticles by Using X-Ray Reflectivity, EXAFS, and Electron Microscopy. *Langmuir* **2006**, *22*, 807−816.
(87) Liu, D.; Lei, W.; Qin, S.; Hou, L.; Liu, Z.; Cui, Q.; Chen, Y. Large-Scale Synthesis of Hexagonal Corundum-Type In_2O_3 by Ball Milling with Enhanced Lithium Storage Capabilities. *J. Mater. Chem. A* **2013**, *1*, 5274−5278.
(88) Buchholz, D. B.; Ma, Q.; Alducin, D.; Ponce, A.; Jose-Yacaman, M.; Khanal, R.; Medvedeva, J. E.; Chang, R. P. H. The Structure and Properties of Amorphous Indium Oxide. *Chem. Mater.* **2014**, *26*, 5401−5411.
(89) Clausen, B. S.; Topsoe, H.; Hansen, L. B.; Stoltze, P.; Norskov, J. K. The Effect of Anharmonicity on the Exafs Coordination-Number in Small Metallic Particles. *Jpn. J. Appl. Phys.* **1993**, *32*, 95−97.
(90) Haneda, M.; Kintaichi, Y.; Inaba, M.; Hamada, H. Additive Effect of Palladium on the Catalytic Activity of $In/TiO_2\text{-}ZrO_2$ for the Selective Reduction of Nitrogen Monoxide in the Presence of Water Vapor. *Bull. Chem. Soc. Jpn.* **1997**, *70*, 2171−2178.
(91) Pettigrew, D. J.; Trimm, D. L.; Cant, N. W. The Effects of Rare Earth Oxides on the Reverse Water-Gas Shift Reaction on Palladium/Alumina. *Catal. Lett.* **1994**, *28*, 313−319.
(92) Föttinger, K. The Effect of CO on Intermetallic PdZn/ZnO and Pd_2Ga/Ga_2O_3 Methanol Steam Reforming Catalysts: A Comparative Study. *Catal. Today* **2013**, *208*, 106−112.
(93) Hamza, A.; Madix, R. Dynamics of the Dissociative Adsorption of Hydrogen on Nickel (100). *J. Phys. Chem.* **1985**, *89* (7), 5381−5386.
(94) Singleton, M. F.; Nash, P. The In-Ni (Indium-Nickel) System. *Bull. Alloy Phase Diagrams* **1988**, *9*, 592−597.
(95) Rahmani, S.; Rezaei, M.; Meshkani, F. Preparation of Highly Active Nickel Catalysts Supported on Mesoporous Nanocrystalline γ-Al_2O_3 for CO_2 Methanation. *J. Ind. Eng. Chem.* **2014**, *20*, 1346−1352.
(96) Weatherbee, G. D.; Bartholomew, C. H. Hydrogenation of CO_2 on Group VIII Metals. II. Kinetics and Mechanism of CO2 Hydrogenation on Nickel. *J. Catal.* **1982**, *77*, 460−472.

DOI: 10.1021/acscatal.8b04848
ACS Catal. 2019, 9, 3399−3412